https://doi.org/10.5194/essd-2024-224
Preprint. Discussion started: 15 July 2024

Open Access Earth System Science Data Discussions

A Moored Array Observation Dataset for Air-Sea·Surface, Upper and Bottom Ocean in the Northern South China Sea during 2014–2015 (MASCS 1.0)

Han Zhang[1,2,3*], Dake Chen[1,2,4], Tongya Liu[1,2], Di Tian[1], Min He[2], Qi Li[2], Jian Liu[2,5]

Correspondence: Han Zhang (zhanghan@sio.org.cn)

[1] State Key Laboratory of Satellite Ocean Environment Dynamics, Second Institute of Oceanography, Ministry of Natural Resources, Hangzhou 310012, China

[2] Southern Marine Science and Engineering Guangdong Laboratory (Zhuhai), Zhuhai 519082, China

[3] State Key Laboratory of Marine Environmental Science, Xiamen University, Xiamen 361102, China

[4] School of Oceanography, Shanghai Jiao Tong University, Shanghai 200030, China

[5] School of Geography and Ocean Science, Ministry of Education Key Laboratory for Coast and Island Development, Nanjing University, Nanjing 210023, China

Abstract. This study reports a moored array dataset (MASCS 1.0) consisting of five buoys and four moorings in the northern South China Sea during 2014–2015. The dataset includes measurements of sea surface meteorological data using two sets of instruments: sea surface waves recorded using a wave recorder, temperature and salinity from the surface to a depth of 400 m, and at 10 m and 50 m above the ocean bottom using conductivity, temperature, and depth (CTD) recorders. It also includes currents from the surface to a depth of 850 m measured using acoustic Doppler current profilers (ADCPs) and at 10 m, 50 m, and 100 m above the surface measured using current meters. Additional measurements were taken for sea surface radiation, air visibility, chlorophyll, turbidity and chromophoric dissolved organic matter at Buoy 3, which was located at the center of the moored array. The dataset captures the effects of tropical cyclones Rammasun, Kalmaegi, Fung-wong, and Hagupit on the moored array, as well as the transition from summer to winter monsoon in the northern South China Sea. The data reveal oceanic processes in the upper and bottom ocean and are valuable for further studies on air-sea interactions and ocean dynamics. All the data described here are made publicly available from https://zenodo.org/records/12635331 (Zhang et al. 2024).

https://doi.org/10.5194/essd-2024-224
Preprint. Discussion started: 15 July 2024

Open Access Earth System Science Data Discussions

1 Introduction

The South China Sea (SCS) is a semi-enclosed marginal sea with a deep basin, making it the largest marginal sea in the tropics, covering nearly 3.5×10^6 km^2. The South China Sea is also the largest marginal sea in the western Pacific, known for its powerful internal tides and abundant internal waves (Alford et al., 2015). Mesoscale eddies in the SCS transport heat and salt (Yang et al., 2019) and modulate sea surface fields (Tan et al., 2023). The background circulations in the SCS are cyclonic in the upper and deep layers, ~~but~~ anticyclonic in the middle layer (Cai et al., 2020). The three factors contributing to the generally cyclonic gyre in the upper ocean of the northern SCS (Jilan, 2004; Liu et al., 2008) are: (1) ~~Q~~quasi-seasonal wind forcing; (2) ~~N~~net water transport into the SCS through the Luzon Strait; and (3) ~~V~~vorticity advection from the Kuroshio. The Kuroshio carrying the northwestern Pacific water intrudes into the SCS through the Luzon Strait (Nan et al., 2015).

The SCS is significantly influenced by atmospheric forcing, such as monsoons (Chen et al., 2023; Chen et al., 2022), tropical cyclones (TCs) (Guan et al., 2024; Shan et al., 2023), and the world's strongest boreal summer quasi-biweekly oscillation (Qi et al., 2023). Marine heat waves (Wang et al., 2022) and variations in air-sea heat flux (Song et al., 2023; Zhang, 2023) are also observed in the northern SCS. ~~The northern SCS~~ features broad continental shelves and steep continental slopes, leading to complex local ocean dynamical processes. For example, breaking internal tides on the continental slope induce along-slope deep sea bottom currents (Xie et al., 2018), and cross-isobathic motion of the water column or synoptic processes (e.g., TCs) induce continental shelf waves, such as topographic Rossby (Wang et al., 2019) and Kelvin mode (Li et al., 2024) waves.

Owing to the complexity of air-sea interaction and oceanic processes in the SCS, local in-situ observations are essential to uncover the phenomena and mechanisms. From 2014 to 2015, a moored array consisting of five buoys and four moorings was deployed in the northern SCS to acquire sea surface meteorological and oceanic data as well as upper and near-bottom oceanic data. This study lists the details of these observations and the resulting dataset. Part of this data have already been used in several studies focusing on air-sea heat flux, ocean temperature-salinity, and dynamical responses to tropical cyclones (Zhang et al., 2016; Zhang et al., 2018; Zhang, 2023), to investigate the influence of typhoons on the pre-existing eddies (He et al., 2024), ocean heat flux by near-inertial waves (Lu et al., 2024), the comparison of microseisms signals generated by typhoons (Lin et al., 2022), the validity of numerical model simulations (Wu et al., 2020; Lim Kam Sian et al., 2020; Lu et al., 2023), and the study of deep ocean energy variability in the SCS (Quan et al., 2022). However, the full potential of this dataset has yet to be realized.

2 Moored array observations

2.1 Position of buoys and moorings

The observation array consisted of five buoys and four moorings in the northern South China Sea (Fig. 1 and 2), deployed from June to September 2014 and recovered from September 2014 to March 2015 (Table 1). The water depth at buoy 1 (B1) and mooring 1 (M1) was approximately 1600 m, while the depths at other stations were greater than 3000 m. Tropical cyclones

https://doi.org/10.5194/essd-2024-224
Preprint. Discussion started: 15 July 2024

Open Access Earth System Science Data Discussions

significantly influenced the observations, as shown in Fig. 1, including Rammasun in July, Kalmaegi and Fung-wong in September, and Hagupit in December. The information regarding these tropical cyclones was obtained from the China Meteorological Administration (https://tcdata.typhoon.org.cn/en/zjljsjj.html), which were deemed more accurate for tropical cyclones affecting China (Lu et al., 2021; Ying et al., 2014). Although the design of some buoys and moorings have already been shown in previous works (e.g. Zhang et al., 2016; Zhang, 2023), the designs of all the stations are redrawn to give more accurate information of the deployment of the instruments (Fig. 1b, Fig. 3).

The horizontal movement of the buoys is minimal during observations, as they primarily move in a circular region with a radius shorter than 0.025° (Fig. 2). However, the rope of buoy 3 (B3) snapped on 15 September 2014, when typhoon Kalmaegi passed over the observation array (Zhang et al., 2016). B3 then became a drifter, initially moving northeastward with circular tracks attributed to the rightward advection and near-inertial surface currents induced by the typhoon. B3 returned to its initial location on 21 September, moved eastward and turned back on 25 September, and followed a southwestward track thereafter. A ship was dispatched to recover B3 on 17 September and it was brought back to land on 21 October. Note that Kalmaegi also increased the horizontal circular movement of B1 to approximately 5 km on the northwest side on 15 September, which was attributed to the northwestward winds on the right side of the typhoon.

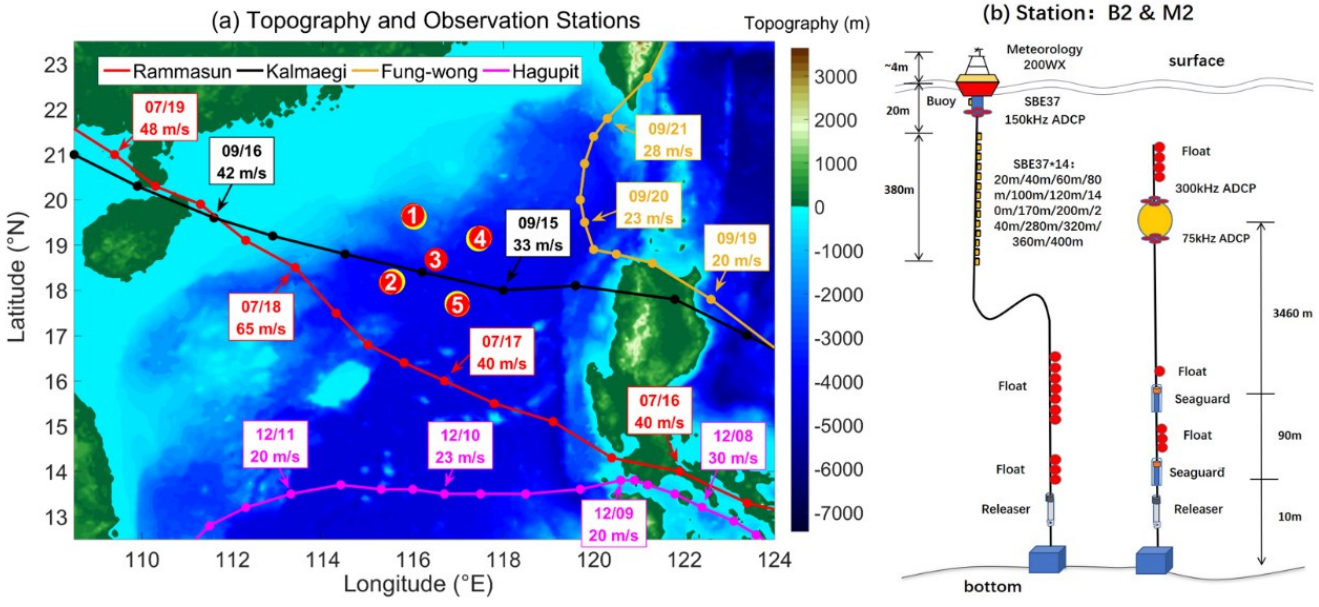

Figure 1: (a): Topography (m) and deployed locations of buoys (red dots) and moorings (yellow dots). (b) Designs of buoy 2 (B2) and mooring 2 (M2) are shown as examples. Tracks of tropical cyclones ~~that may influence the observation array~~ are shown (colored lines), along with their positions every 6 h (dots), ~~including tropical cyclones Rammasun (red), Kalmaegi (black), Fung-wong (orange), and Hagupit (purplish red).~~ The text boxes indicate the dates and sustained maximum wind speed at UTC 00:00 on each date. Note that 8 h should be added to convert to the BJT time shown in this work.

https://doi.org/10.5194/essd-2024-224
Preprint. Discussion started: 15 July 2024

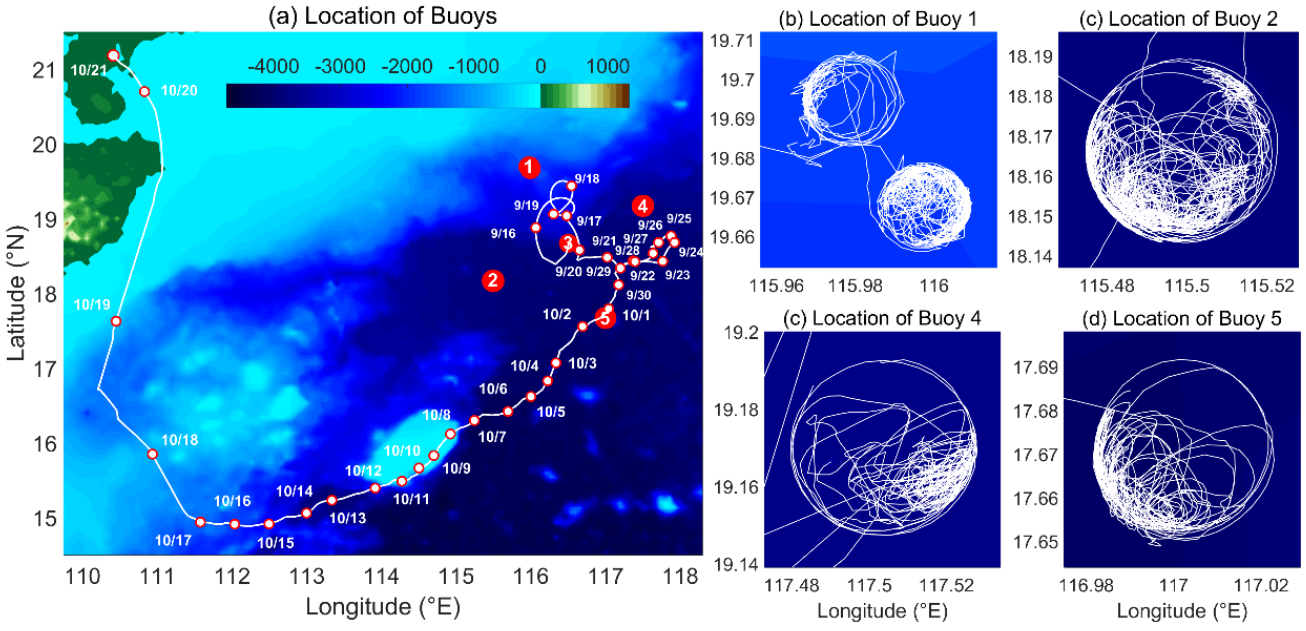

80 **Figure 2: Distribution of the buoy locations. White lines represent the buoy tracks.**

Table 1. Information of the observation station

Station	Deployed Longitude (E)	Deployed Latitude (N)	Estimated Water Depth (m)	Time Range
Buoy 1 (B1)	115°59’49.8”	19°40’04.8”	1625	2014.06.16–2014.10.15
Buoy 2 (B2)	115°29’53.5”	18°09’59.3”	3710	2014.07.21–2015.01.27
Buoy 3 (B3)	116°30’33.9”	18°40’40.2”	3310	2014.09.11–2014.10.21
Buoy 4 (B4)	117°30’11.4”	19°10’01.7”	3430	2014.06.11–2014.09.24
Buoy 5 (B5)	116°59’55.7”	17°39’58.8”	3930	2014.06.05–2014.11.13
Mooring 1 (M1)	116°01’17.1”	19°37’28.7”	1630	2014.06.08–2015.03.28
Mooring 2 (M2)	115°32’57.8”	18°11’29.5”	3740	2014.06.14–2015.03.15
Mooring 4 (M4)	117°27’16.8”	19°08’24.9”	3410	2014.06.09–2015.03.29
Mooring 5 (M5)	116°58’50.8”	17°42’18.1”	3930	2014.06.05–2015.03.30

https://doi.org/10.5194/essd-2024-224
Preprint. Discussion started: 15 July 2024

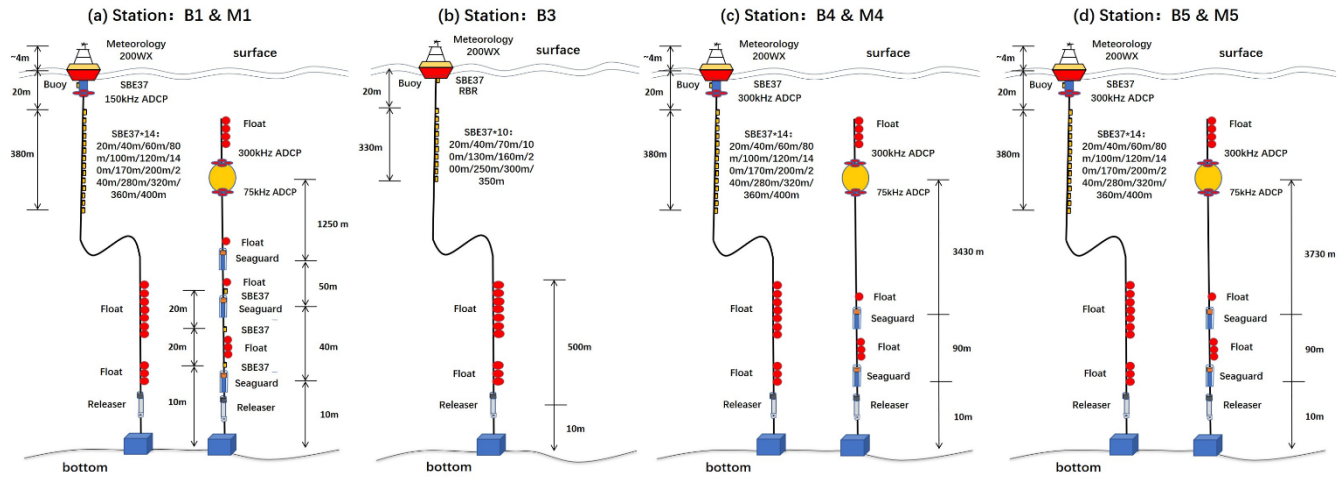

Figure 3: Design of stations 1, 3, 4, and 5. Note that all the stations consist of both a buoy and a mooring, except station 3, which only has a buoy.

Table 2. Observation data details at each station

	Stations	Elements	Equipment and position	Time Resolution
Buoy Location 1	B1-B5	Longitude (°E), Latitude (°N)	GPS sensor 1	1 h
Buoy Location 2			GPS sensor 2	
Buoy Location 3	B1, B2, B4, B5		GPS sensor 3	1 h (B1, B4), 3 h (B2) or 6 h (B5)
Meteorological data 1	B1-B5	Air temperature (°C), Air Pressure (hPa), Compass (°), Wind speed (m/s, average and maximum), Wind direction (°, average and maximum), Rainguage (mm), Compass (°)	Meteorological sensors at 4 m height from sea surface	12 min (B2) or 1 h (B1, B3, B4, B5)
Meteorological data 2			Auto meteorological station (200WX) at 4 m height from sea surface	
Current 1	B1, B2, B4, B5, M1, M2, M4, M5	Speed (cm/s), Direction (°), Vertical velocity (cm/s) Temperature Bin (m), Real-time and designed depth of the ADCP (m, Depth and Depth 0)	Downward looking for layer 1, 3, and uplooking for layer 2	3 min (300 and 150 kHz ADCP) or 15 min (75 kHz ADCP)
Current 2	M1, M2, M4, M5	Speed (cm/s), Direction (°)	Seaguard at 10 m (M1, M2, M4, M5), 50 m (M1) and 100 m (M1, M2, M4, M5) from ocean bottom	10 min

https://doi.org/10.5194/essd-2024-224
Preprint. Discussion started: 15 July 2024

Sea temperature, salinity and pressure	B1, B2, B4, B5, M1	Temperature (°C), salinity (psu), pressure (hPa), depth (m)	SBE-37 with design depth (m) at buoys: 20, 40, 60, 80, 100, 120, 140, 170, 200, 240, 280, 320, 360, 400. SBE-37 with design depth 10 m and 50 m above the bottom at M1	2 min
Sea Surface Waves	B1, B4	Wave height (m, Significant and Maximum), Peak period (s), Mean wave direction (°), Wave spread	Wave gauge at sea surface (0 m)	1 h
Radiation (W/m^2)	B3	Short wave (upward, downward), Long wave (upward, downward), Wave temperature (°C)	Wave Radiometer at 4 m height from sea surface	1 h
Visibility (VIS, km)		Air visibility (km)	Visibility meter at 4 m height from sea surface	
Biochemistry data		Water pressure (hPa), Turbidity (V, two sensors), Chlorophyll (ug/L, Chla), Colored dissolved organic matter (ppb, CDOM)	RBR sensors at sea surface (0 m)	12 min

2.2 Dataset description

The dataset is composed of 52 files in netcdf file (.nc) format containing air and ocean observation data as well as the positions of the buoys during the period of 2014–2015, along with a metadata file in .txt format to give a brief introduction of the data. The observation instruments were calibrated before deployment and the observation data are transformed directly to netcdf files after output from the observation instruments, with the units and FillValues labeled. No special modification or say quality control was applied in order to keep the original output data unchanged. All the files include time values both Coordinated Universal Time (UTC) and local time which is eight hours ahead of the Coordinated Universal Time (UTC +8) since 0000-01-01 00:00:00. The local time is also called China Standard Time (CST) or Beijing Time (BJT). The location data includes longitude (°E) and latitude (°N) observed by Global Positioning System (GPS) sensors. There were three GPS sensors on buoys 1, 2, 4, and 5, and two GPS sensors on buoy 3. Location-1 data was obtained from the main GPS sensors on the body of the buoys, Location-2 data was obtained from the GPS sensors approximately 4 m above the sea surface, and Location-3 data was obtained from the low-frequency GPS sensors at the bottom of the buoys (approximately 0 m).

The air data includes observations approximately 4 m above the sea surface from meteorological sensors (Meteorology data) and the ~~200WX~~ automatic meteorological station (200WX data). The meteorology data includes air average wind speed (m/s), average wind direction (°), maximum wind speed (m/s), maximum wind direction (°), temperature (°C), humidity (%), pressure (hPa), rainguage (mm), and compass (°) of the station. The 200WX data are similar to the meteorology data, but does not include any rainguage data. The direction of wind indicates the direction of the incoming wind; for example, 0° indicates

https://doi.org/10.5194/essd-2024-224
Preprint. Discussion started: 15 July 2024

wind passing from north to south, and 90° indicates wind passing from east to west. The compass indicates the direction of the compass on the meteorological sensors or stations, which refers to the attitude of the sensors or stations. For the meteorology data of buoy 3, there are also upward and downward short- and long-wave radiation (W/m^2), air visibility (km), and temperature observed by the radiation meter (°C, wave temperature).

The ocean data includes sea surface waves observed by wave recorder (Wave data), temperature, salinity, and pressure observed by Seabird ~~(SBE)~~ CTD (SBE data), and currents observed by acoustic doppler current profilers (ADCP) data and current meters (Seaguard data). Sea surface wave data includes significant wave height (m), maximum wave height (m), mean wave direction (°), peak period (s), and wave spread. Wave recorders were deployed on buoys 1, 4, and 5, but the wave recorder on buoy 5 broke down, resulting in low-quality data. Consequently, only sea surface wave data from buoys 1 and 4 were included in the ocean data. SBE data includes temperature (°C), salinity (psu), and pressure (hPa) observed by SBE-37 CTD sensors. Serial 1 to 15 in the SBE data refers to the SBE-37 sensors from the surface to the ocean bottom. All SBE sensors are deployed on the buoys, except for three SBE-37s on the moorings located near the ocean bottom (Fig. 1(b) and 2). Note that the SBE-37 strings on buoys 1 and 3 were lost during observation, so only SBE data at the sea surface located at the bottom of the buoy (Temperature1, Salinity1, and Pressure1) was obtained. Two SBE-37s on buoy 4 broke down during observation, resulting in data from only 13 SBEs. The ADCP data consists of current speed (cm/s Speed), current direction (° direction), temperature observed by ADCP (°C temperature), depth of the ADCP (m depth), designed depth (depth0), and bin intervals of the ADCP observation (m bin). The Seaguard data includes current speed (cm/s speed) and current direction (° direction). Unlike wind direction, current direction indicates the direction of the current flow, for example, 0° indicates current passing from south to north, and 90° indicates the current passing from west to east. Negative Bin values refer to downward-looking ADCPs and vice versa. ADCPs on the buoys (ADCP 1) were downward-looking, located at the sea surface (approximately 0 m), so their observation range was depth0 + bin. The ADCP data on moorings consist of upward-looking (ADCP 2) and downward-looking (ADCP 3) observations with ranges depth + Bin, as the depth of the ADCPs at moorings varies during observation. Note that buoy 3 did not have ADCP or Seaguard observation (see Fig. 3 and Table 2), and ADCP at buoy 5 broke down and no data obtained.

3 Results

The data at station 2 (B2 and M2) were long and more complete relative to other stations, and is shown first to provide an example of the observations at the stations. Subsequently, observations differing from station 2 are also shown, including near-bottom observations at B1, sea surface waves at B1 and B4, and the observations at B3 after its rope snapped on 15 September, causing it to become a drift.

https://doi.org/10.5194/essd-2024-224
Preprint. Discussion started: 15 July 2024

3.1 Sea surface air and ocean observation at station 2

The prevailing wind direction was approximately 200° (nearly south wind) from late July to mid-August, then shifted primarily in the range of 20°–80° (nearly northeast wind) after October, with wind direction variations during September (Fig. 4(b), (d)). This finding indicates that the transition occurred from local summer to winter monsoon, with September as the transition month. Average wind speed is less than 10 m/s during July and August, often exceeding 10 m/s after October (Fig. 4(a), (c)), indicating that the winter monsoon was stronger than the summer monsoon at B2. B2 likely traveled through the eye of typhoon Kalmaegi, with two peaks in wind speed accompanied by minimum air pressure (Zhang et al., 2016). Note that typhoon Kalmaegi and severe tropical storm Fung-wong during September significantly influenced wind direction at B2, with wind direction turning counter-clockwise near September 15 and 21, consistent with B2 being on the left side of both TCs.

B2 also recorded a drop in sea surface air and ocean temperature (Fig. 4(g), (i)) from summer to winter, ranging from approximately 28.5 °C to 30.5 °C in August, decreasing from approximately 29 °C to approximately 27 °C in October, and continuing to decrease further. Surface air temperature was slightly lower than sea surface temperature during the observation period, indicating local sensible heat flux from the ocean to the atmosphere, as water cooled slower than air during autumn. The diurnal variation of temperature, attributed to daytime solar radiation heating and nighttime outward longwave radiation cooling, and the deepening of the ocean mixed layer, were also captured by the observations due to their high time resolution (2 min). Typhoon Kalmaegi and Fung-wong successively decreased sea surface air and ocean temperatures during September, with Kalmaegi suddenly decreasing sea surface temperature by approximately 2.5 °C, as B2 was located in the core cooling area on the right side of the typhoon track.

Rainguage data was measured by a tipping bucket rain gauge, with a maximum measurement of 255 mm. The bucket empties when full (255 mm) and measurement starts from 0 mm again. Rain rate can be calculated by dividing the difference in rainguage values by the time interval. Significant rainfall events were recorded near 2 August, 6 September, 15 September, and 21 September. The strong rainfall near 15 September and 21 September was induced by typhoon Kalmaegi and severe tropical storm Fung-wong. Note that evaporation also affected rainguage values, which decreased slowly over time without precipitation, indicating that rainguage data reflected precipitation and evaporation. Sea surface salinity increased from approximately 33.3 psu near 1 October to approximately 33.8 psu near 10 November (Fig. 4(i)), owing to little rainfall during this period, with salinity primarily controlled by evaporation.

There were some consistencies and differences between the two sets of meteorological observations. The average and maximum wind data in the Meteorology and 200WX datasets are consistent, while the wind direction measured by the meteorological sensor may have malfunctioned, as average wind direction suddenly turned to approximately 180° and maximum wind direction varied rapidly between 0° and 360° after 15 November (Fig. 4(b), (d)). Air pressure measurements from the meteorology and 200 WX datasets are consistent before 27 August, with the diurnal variation of air pressure observed by the meteorological sensor amplifying and becoming inconsistent with 200WX observations after 27 August (Fig. 4(f)). The sensitivity of air temperature measurements by the 200WX was greater than the meteorological sensor, with larger amplitude

https://doi.org/10.5194/essd-2024-224
Preprint. Discussion started: 15 July 2024

Open Access Earth System Science Data Discussions

diurnal variations. Air humidity measured by the meteorological sensor was greater than that measured by the 200WX, ranging from 0 % to 10 %. Both two sets of meteorological observations showed missing data about 5 days near 6 October, which may due to the malfunction of the instruments or data recording.

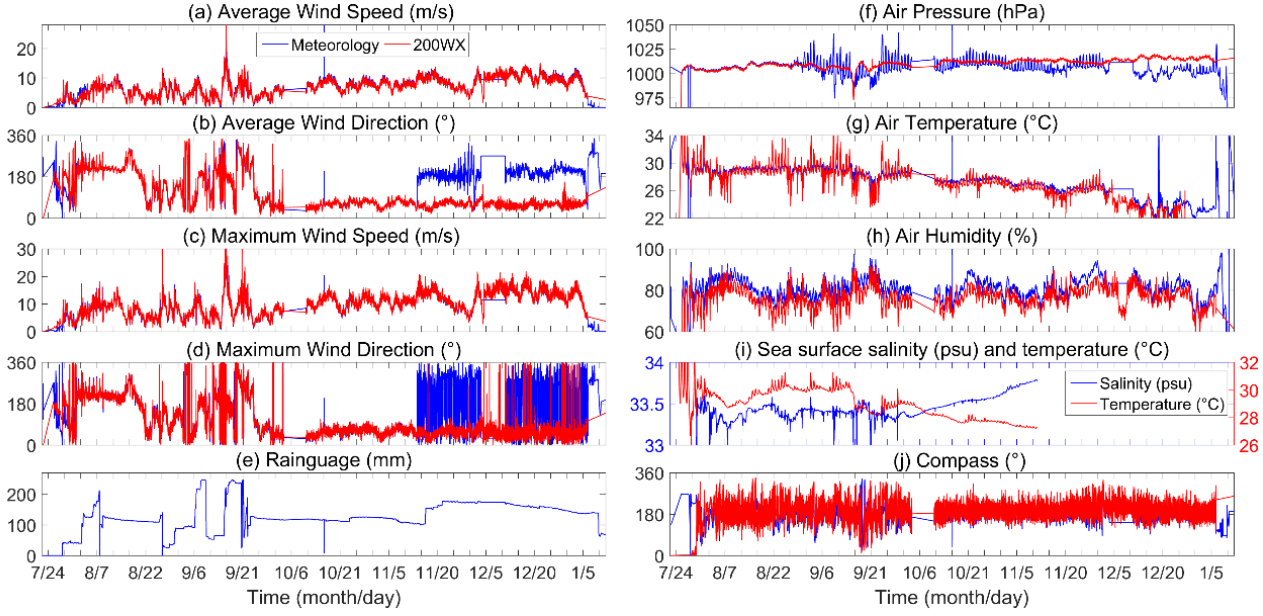

Figure 4: Observation at Buoy 2. Average and maximum wind speed (a, b m/s) and direction (c, d °), rainguage (e mm), air pressure (f hPa), air temperature (g °C), air humidity (h %), sea surface salinity (i psu), sea surface temperature (i °C), and buoy compass (j °). Blue and red lines are data observed by meteorological sensors and the 200WX automatic meteorological station, approximately 4 m above the sea surface, while blue and red lines in (i) represent salinity and temperature observed by the SBE-37 sensor at the buoy bottom (approximately 0 m). Wind directions indicate the direction from which the wind originates.

3.2 Current, temperature, and salinity observation at station 2

At station 2, the current observations at the mooring (Fig. 5(b–d)) were longer than those at the buoy (Fig. 5(a)), as well as the temperature and salinity (Fig. 6) observations at the buoy, due to the deployment and recovery times. The upward-looking 300 kHz ADCP (Fig. 5(b)) and the SBE-37 recorder at the bottom of the buoy (Fig. 6) stopped working near 11 November, while data quality from the downward-looking 75k Hz ADCP at the mooring decreased especially in year 2015, with some missing data at several bins (Fig. 5(b)). Although the length of the chain of SBEs was 400 m, the observation range of temperature and salinity was primarily shorter than 400 m, as the rope swung and tilted during observation, especially the deepest observation depth decreased to ~200 near 21 September under the influence of typhoon-induced near-inertial waves after Kalmaegi. Similarly, the positions of ADCPs at moorings also moved vertically due to the tilt of the mooring rope, especially when influenced by near-inertial waves from Rammasun in July and Kalmaegi in September.

Horizontal currents induced by diurnal and semi-diurnal tides were captured by ADCPs and Seaguards, along with diurnal and semi-diurnal vertical variations of temperature and salinity isolines. The upper ocean background current speed was primarily <20 cm/s, significantly increasing after tropical cyclones, e.g., Rammasun in July, Kalmaegi in September, and

https://doi.org/10.5194/essd-2024-224
Preprint. Discussion started: 15 July 2024

Open Access Earth System Science Data Discussions

Hagupit in December, with mixed layer current speed reaching approximately 150 cm/s after Kalmaegi (Zhang et al., 2016). The downward propagation of near-inertial waves after tropical cyclones was also evident in the ADCP data. For example, typhoon Kalmaegi immediately strengthened near-inertial mixed layer currents and kinetic energy, which then propagated horizontally and vertically with the dispersion of near-inertial waves and regulation by background vorticity (Lu et al., 2023; Lu et al., 2024; Zhang et al., 2016). Near-bottom currents were mainly <10 cm/s, while near-bottom flow turned from northeastward to southeastward after the influence of typhoon Rammasun.

Upper ocean temperature decreased monotonously from the surface (approximately 0 m) to approximately 400 m, and salinity exhibited a "low-high-low" vertical structure with a maximum of approximately 34.5 psu from approximately 100 m to approximately 250 m. There is long-term upper ocean cooling and a decrease in salinity from summer to winter (Fig. 5), especially after mid-October. Kalmaegi reduced sea surface temperature by approximately 1.9 °C at its maximum, with a subsurface cold anomaly of approximately 1.1 °C at its maximum (Zhang et al., 2016) owing to its proximity to the typhoon track, where upper ocean temperature was primarily modulated by typhoon-induced mixing and upwelling (Zhang, 2023; Zhang et al., 2018). Vertical variations of temperature and salinity were also influenced by processes such as eddies, fronts, and flows (Liu et al., 2017; Lu et al., 2024), but these are not pursued further here. The downward propagation of warm or freshwater anomalies from the surface, along with the diurnal cycle of the near-surface mixed layer, can also be observed.

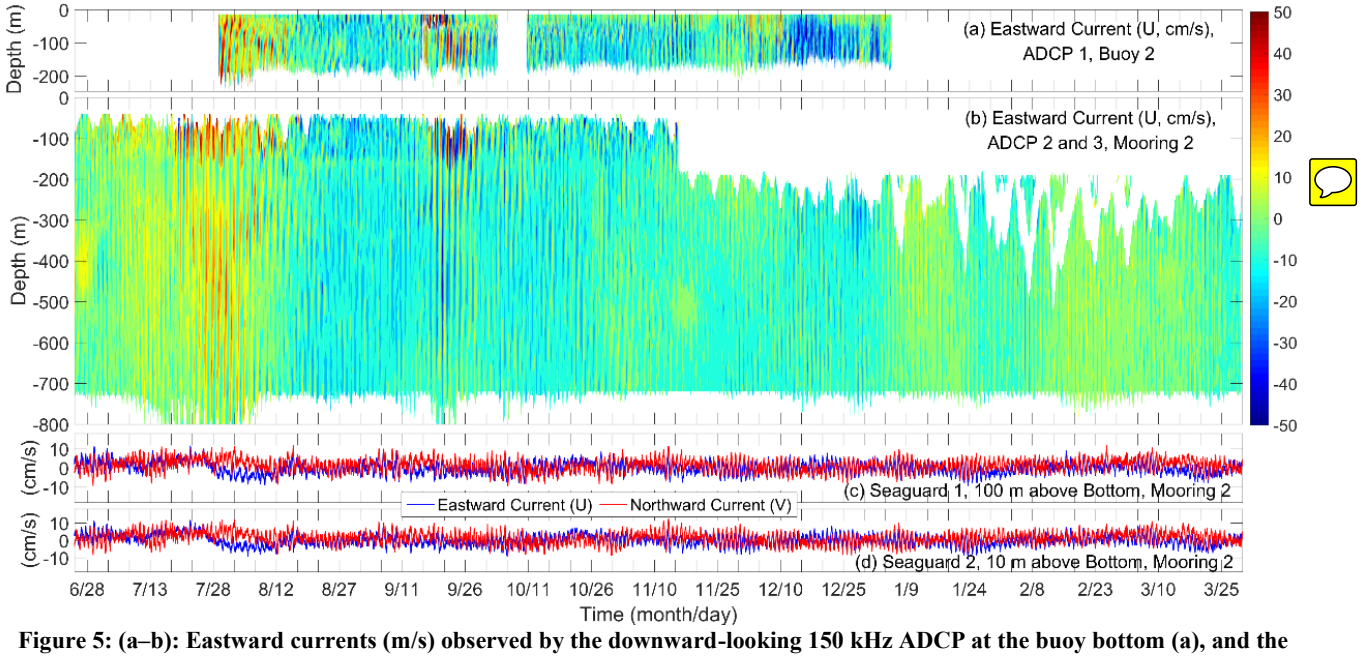

Figure 5: (a–b): Eastward currents (m/s) observed by the downward-looking 150 kHz ADCP at the buoy bottom (a), and the combination of upward-looking 300 kHz and downward-looking 75 kHz ADCP at the mooring (b). (c-d) Eastward (U) and

https://doi.org/10.5194/essd-2024-224
Preprint. Discussion started: 15 July 2024

northward (V) currents observed by Seaguard current meter at 100 m (c) and 10 m (d) above the ocean bottom.

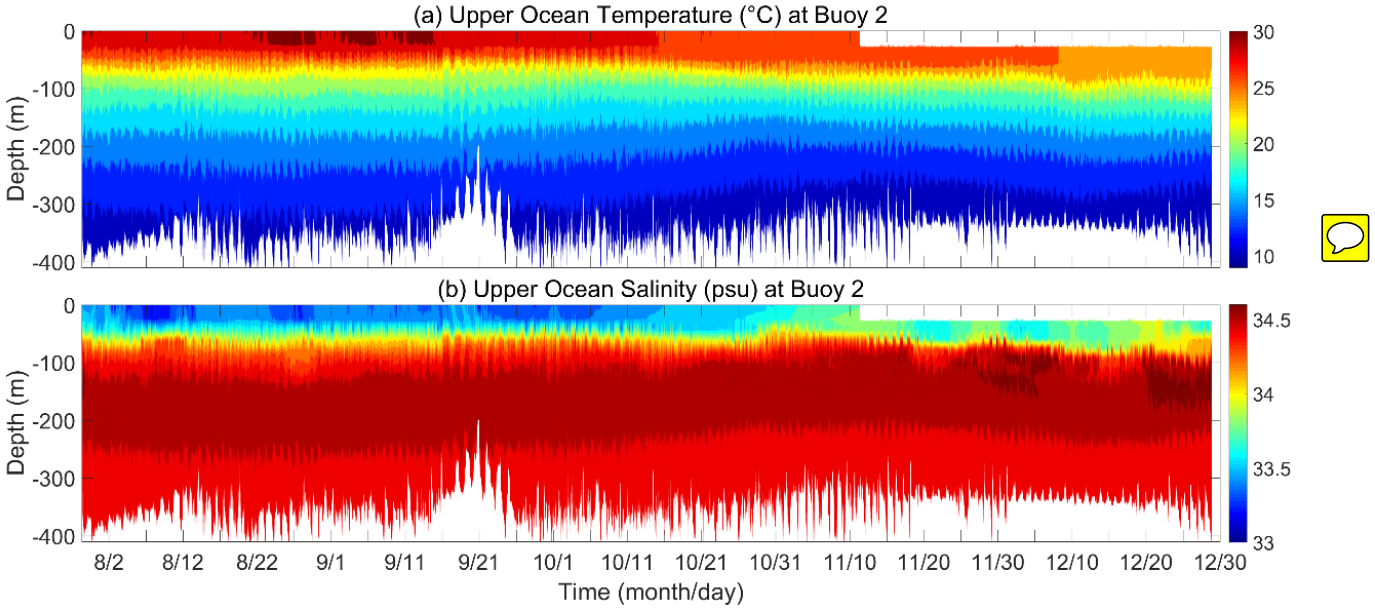

Figure 6: Upper ocean temperature (a, °C) and salinity (b, psu) observed by the chain of SBE-37 sensors at buoy 2.

3.2 Near bottom observation at mooring 1

The instruments at M1 differed from those at other moorings, so their observations are analyzed and discussed here. The variation of near-bottom pressure observed by the three SBEs at approximately 10 m, 30 m, and 50 m above the ocean bottom is very small (Fig. 7(~~a~~)), indicating minimal swing and tilt of the rope near the bottom of M1. The water pressure at approximately 10 m above the bottom was approximately 1710 hPa, corresponding to a depth of approximately 1690 m, indicating that the water depth of M1 was approximately 1700 m (true depth) rather than approximately 1630 m (designed depth). The temperature varied from 2.5 °C to 2.7 °C, and salinity is close to 34.6 psu at the three SBEs (Fig. 7(b), (c)). The temperature, salinity, and currents observed from the three SBEs and Seaguards were very close, indicating a uniform near-bottom layer greater than 100 m. However, the current at 100 m above the bottom differed from the other two layers during 29 July to 12 August and 20 December to 13 December, when near-bottom flow also turned at M1, possibly influenced by super typhoons Rammasun and Hagupit.

https://doi.org/10.5194/essd-2024-224
Preprint. Discussion started: 15 July 2024

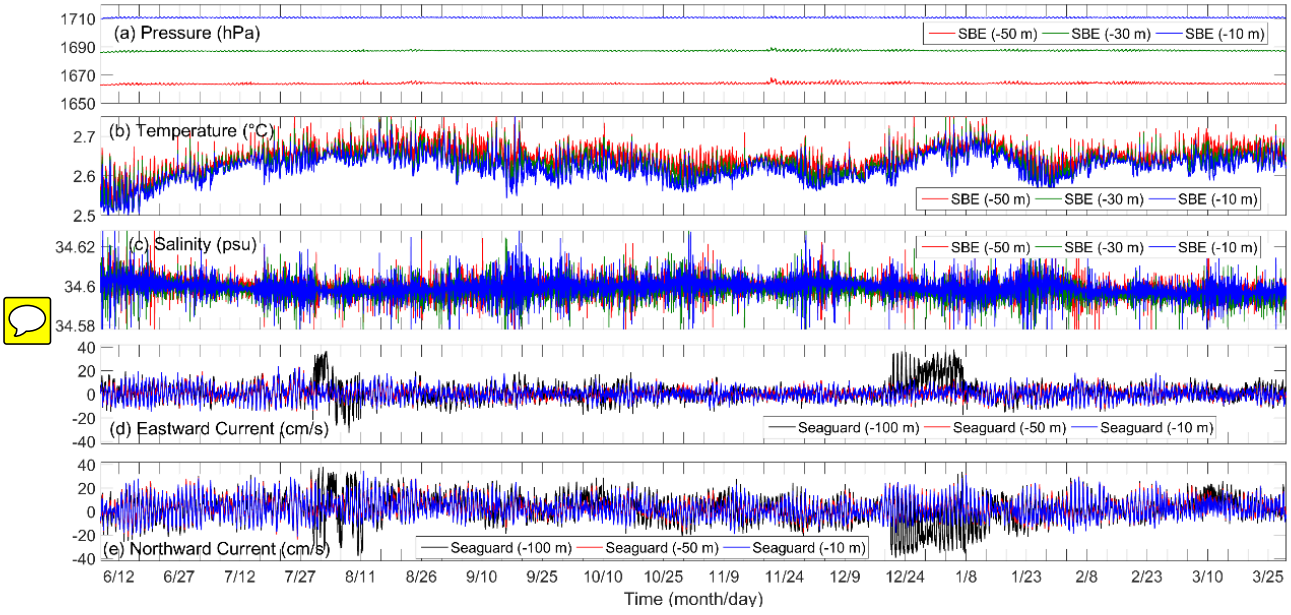

Figure 7: (a–c): Pressure (hPa a), temperature (°C b), and salinity (psu c) observed by the SBE-37 at the mooring at approximately 50 m (red), 30 m (green), and 10 m (blue) above the ocean bottom. (d-e) Eastward current (cm/s) and northward current observed by the seaguard current meter at the mooring at approximately 100 m (black), 50 m (red), and 10 m (blue) above the ocean bottom.

3.3 Sea surface waves

Sea surface waves observed at B1 and B4 also merit further explanation. The variations of sea surface waves from the two wave gauges at B1 and B4 are similar (Fig. 8), indicating that the characteristic of the sea surface waves at the observation array were comparable. The observation at B1 were longer than B4, but with some miss recording near 1 August to 17 August. Sea surface waves were mainly controlled by sea surface winds, e.g., monsoon and tropical cyclones. During the summer monsoon (before September), significant wave height was primarily <2 m, maximum wave height <3 m, peak period <10 s, and mean wave direction was close to 180° (southward). During the winter monsoon (after October), significant and maximum wave heights increased to >3 m and >5 m, respectively, as well as peak period > 10 s and mean wave direction nearly 90° (eastward). Wave spread ranged from 20 to 80 throughout the observation period of the two wave gauges.

Tropical cyclones strongly influenced local sea surface waves. Wave height of sea surface significantly increased to approximately 5 m, 10 m, and 3 m, while maximum wave height reached approximately 8 m, 15–18 m, and 5–6 m due to the influence of tropical cyclones Rammasun, Kalmaegi, and Fung-wong, respectively. Sea surface wave height increased rapidly in one day, along with a clockwise rotation of mean wave direction and an increase in peak period, then returned to background conditions within approximately three days, with the mean wave direction rotating counterclockwise and a decrease in peak period.

https://doi.org/10.5194/essd-2024-224
Preprint. Discussion started: 15 July 2024

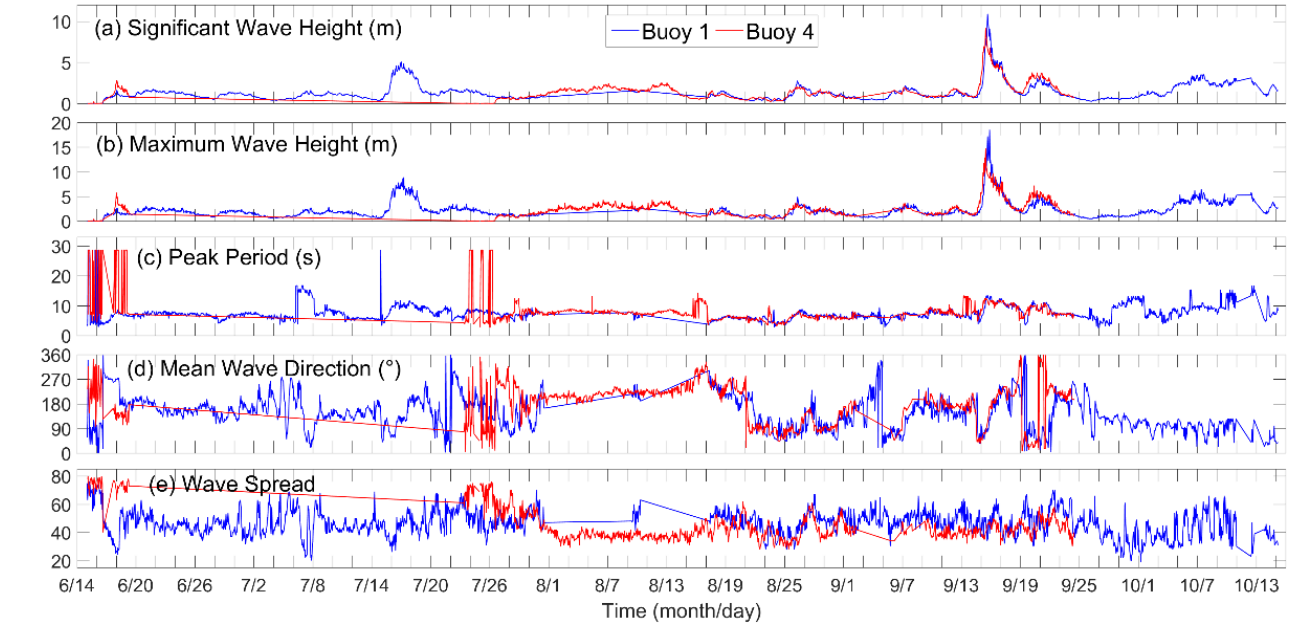

Figure 8: Significant wave height (a, m), maximum wave height (b, m), peak period (c, s), mean wave direction (d, °), and wave spread observed by the wave recorders at the bottom of buoys 1 (blue) and 4 (red).

3.4 Observation at buoy 3

As the rope of B3 snapped on 15 September, causing the buoy to became adrift (Fig. 2), it is important to describe B3 observations in this section, which partly reflects the air-sea conditions in region B3 (Figs 9 and 10).

The average and maximum wind speeds increased to approximately 20 m/s and 25 m/s, respectively, during Kalmaegi, with wind direction changing rapidly. The average and maximum wind speeds reached approximately 10 m/s during Fung-wong, with the wind direction rotating counterclockwise, as B3 was on the left side of the TC track. In October, the wind direction was primarily close to 0°, consistent with B2 (Fig. 4), indicating that the local region was controlled by the monsoon from nearly north to south. Rainfall was strong during Kalmaegi (approximately 250 mm) and Fung-wong (approximately 200 mm), accompanied by low air pressure (980 hPa and 1000 hPa), while there was little rainfall, and air pressure increased to more than 1100 hPa after that. The diurnal variation of air pressure can also be found in the observation. Sea surface temperature continuously reduced from ~30°C to ~27.5°C and ~26.5°C after Kalmaegi and Fung-wong, and then recovered back to ~29°C in October. Note that surface air temperature was 1-3 °C colder than sea surface temperature during the observation, indicate that there was sensible heat flux from ocean to air in Autumn along the track of B3. Air humidity was 85% to 100% during the influence of Kalmaegi and Fung-wong (14 to 25 September), and then continuously decreased to approximately 70% in October, consistent with the fact that the TC-induced cold wake results in reduced rainfall and sea surface humidity (e.g., Ma et al., 2020). Air visibility was approximately10 m when B3 was deployed, then decreased to approximately 1 m due to cloud cover and adverse sea surface conditions from typhoon Kalmaegi, rapidly increased to

https://doi.org/10.5194/essd-2024-224
Preprint. Discussion started: 15 July 2024

approximately 16 km on 15 September due to the passage of the typhoon eye. Clear sky returned near 17 September, while subsequent tropical cyclone Fung-wong increased air visibility at B3 to approximately 16 km again on 20 September, lasting until 22–23 September.

B3 was the only buoy equipped with a radiometer. The maximum shortwave radiation observed by the upward sensor was approximately 1900 W/m^2 near noon, when solar radiation was strongest, significantly reduced by cloud cover from tropical cyclones from 13 to 23 September, and moderately reduced by local cloud cover in October. Conversely, the shortwave radiation observed by the downward sensor was much (one order) smaller than the upward shortwave radiation, indicating a minimal reflection of solar radiation. Similarly, the longwave radiation observed by the upward and downward sensors was close to 0 W/m^2 and approximately −50 W/m^2, respectively, indicating that longwave radiation was primarily from the ocean to the atmosphere, with minimal contribution from the atmosphere to the ocean. The sea surface temperature (Fig. 10(d)) decreased from approximately 30 °C to approximately 27 °C after Kalmaegi, recovering to approximately 29 °C in October. The wave temperature (Fig. 10(c)) followed a similar variation pattern with air temperature (Fig. 9(a)) and sea surface temperature, with significant diurnal variation. It is noteworthy that sea surface salinity (Fig. 10(d)) increased from approximately 33.5 psu to approximately 33.7 psu due to typhoon Kalmaegi, despite strong rainfall (Fig. 9(e)). The variation in sea surface salinity was consistent with the rainguage data, except for a decrease in salinity from 3 to 5 October. There were some recording errors of sea surface temperature and salinity after 5 October (Fig. 10(d,e)) with sudden change of the values.The SBE and Richard Brancker Research (RBR) sensors were deployed at approximately 1.3 to 1.6 m from the surface, with pressures nearly 1.3 hPa–1.6 hPa (Fig. 10(f)). Chlorophyll observed by the RBR sensor (Fig. 10(g)) showed diurnal variation, increasing from approximately2 ug/L to approximately 2.5 ug/L after Kalmaegi and Fung-wong, then returning to approximately 2 ug/L afterward. Turbidity observed by the first sensor (Fig. 10(h)) is more than 0.05 V before September 15, then decreased to approximately 0.005 V, making it difficult to determine whether the decrease is attributable to Kalmaegi, which made the sea surface cleaner, or damage to the turbidity sensor after B3's rope snapped. Conversely, turbidity observed by the second sensor (Fig. 10(i)) remained near 4.4569 throughout the observation period of B3 (Fig. 10(i)). Chromophoric dissolved organic matter (CDOM, Fig. 10(j)) gradually increased from 1.88 ppb in September to 2.1 ppb by mid-October.

https://doi.org/10.5194/essd-2024-224
Preprint. Discussion started: 15 July 2024

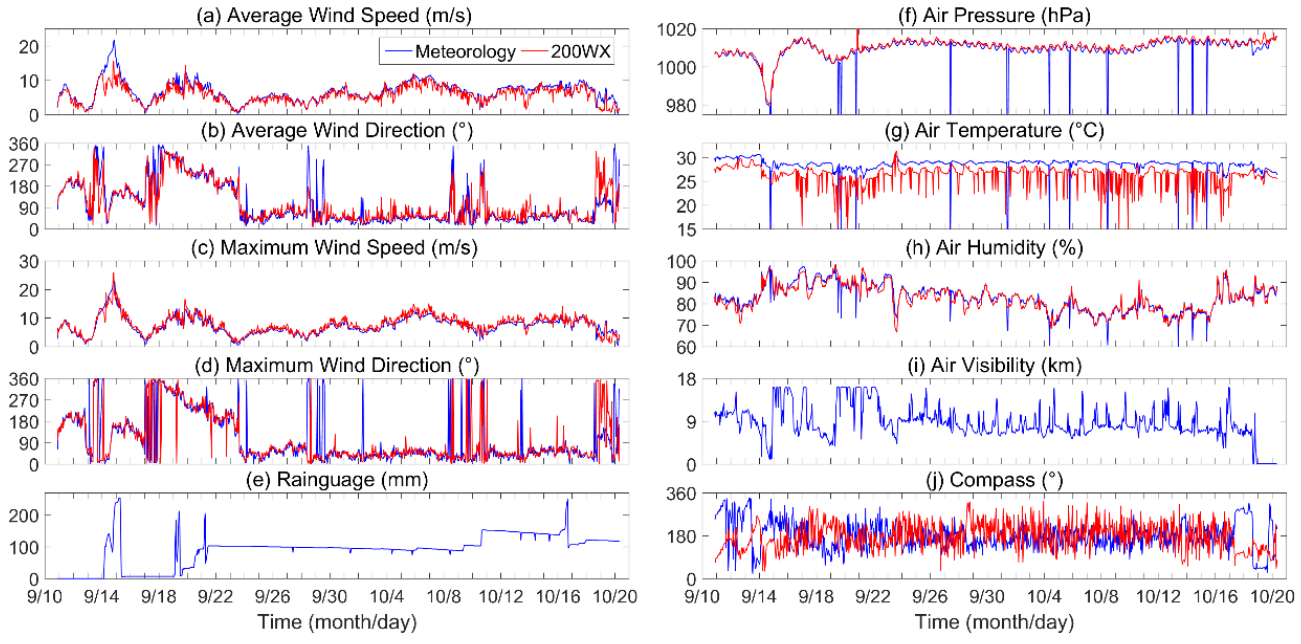

Figure 9: Similar to Figure 4 but for buoy 4. Note that (i) is air visibility (km) observed by a visibility meter located 4 m above the sea surface.

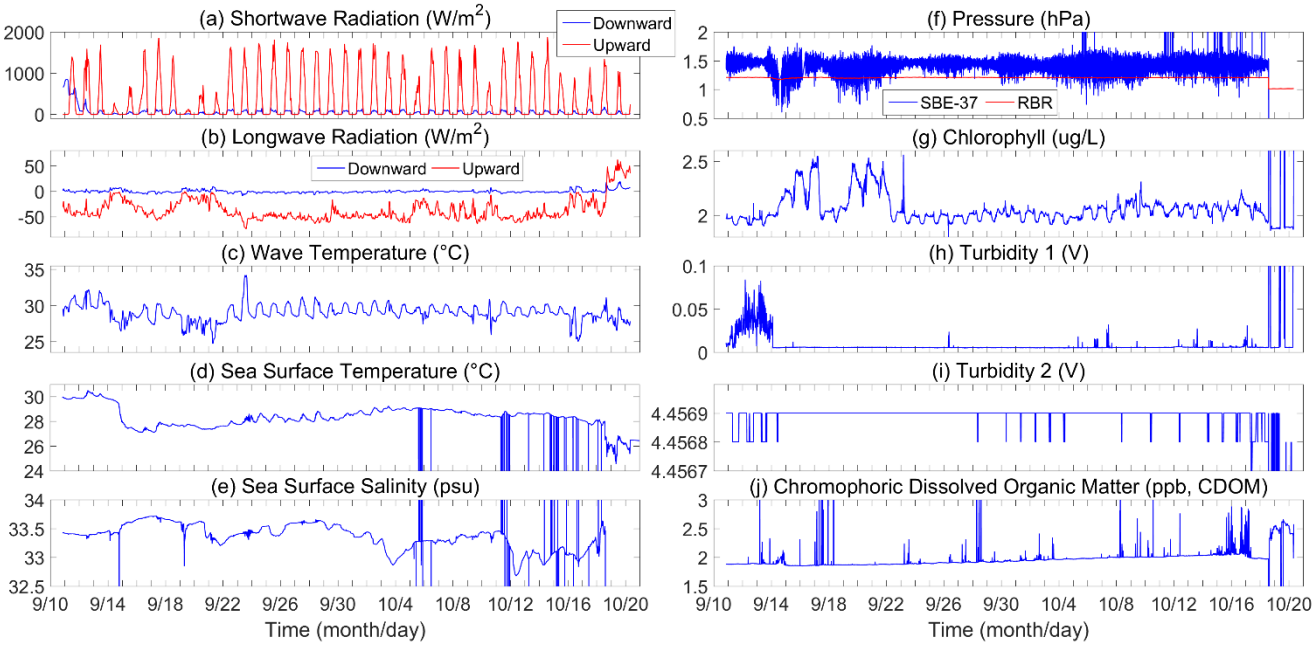

https://doi.org/10.5194/essd-2024-224
Preprint. Discussion started: 15 July 2024

Figure 10: Observation at Buoy 3. (a–c): Shortwave radiation (a, W/m^2) and longwave radiation (b, W/m^2) observed by upward (red) and downward (blue) radiation sensors and the wave temperature (c, °C) observed by the radiometer. (d–f): Sea surface temperature (f, °C), salinity (g, psu), and pressure (h, hPa, blue) observed by SBE-37, with pressure (h, hPa, red) observed by RBR sensors. (g–j): Chlorophyll (g, ug/L), turbidity observed by two sensors (g–h, V), and chromophoric dissolved organic matter (j, ppb, CDOM). Radiometer is located 4 m above the sea surface, while the SBE-37 and RBR sensors are at the bottom of buoy 3 (approximately 0 m).

4. Data availability

All data are made publicly available through Zenodo repository with the address: https://zenodo.org/records/12635331 (Zhang et al. 2024). The data will also be publicly available at the website of the Southern Marine Science and Engineering Guangdong Laboratory (Zhuhai) (http://www.hellosea.org.cn/#/metadataDetail/en-US?detailId=8f32902492b84dc1a80f0f717a7c827e) if the manuscript published. This study provides a detailed description of the dataset, which includes a time series of sea surface meteorological elements, sea surface waves, ocean temperature, salinity, and currents collected from a moored array consisting of five buoys and four moorings during 2014–2015. Meteorological elements included wind, temperature, pressure, rainguage, and humidity data. In addition, data from the buoy at the center (B3) included sea surface visibility, radiation (shortwave and longwave), and biochemistry observations (chlorophyll, turbidity, and colored dissolved organic matter).

5 Conclusions

This study presents an observation dataset from a moored array consisting of five buoys and four moorings in the northern South China Sea during 2014–2015 (MASCS 1.0). The tracks of each buoy were recorded by global positioning system (GPS) sensors with outputs every 1 h, 3 h, or 6 h. Each buoy was equipped with a few meteorological sensors and an automatic meteorological station (Airmar 200WX) located approximately 4 m above the sea surface, with outputs every 12 min (B2) and 1 hour (B1, B3-B5). A string of Sea-Bird Scientific 37 (SBE-37) conductivity, temperature, and depth (CTD) recorders was also deployed from approximately 0 m to approximately 400 m with outputs every 2 min. ADCPs were deployed at both buoys and moorings to measure horizontal currents from approximately 0 m to approximately 850 m, with outputs every 3 min (300 and 150 kHz ADCP) or 15 min (75 kHz ADCP). Seaguard current meters recorded currents at 10 m and 100 m from the ocean bottom at the moorings, with outputs every 10 min, while M1 was equipped with extra SBEs (2-min resolution) at 10 m and 50 m above the ocean bottom, and a Seaguard (10-min resolution) at 50 m above the ocean bottom. Note that some instruments broke down or were lost during observation, resulting in no data recovery or deficiencies.

TRIAXYS^{TM} OEM wave recorders, which measured the significant and maximum wave height, wave peak period, mean wave direction, and wave spread with output every 1 h, were deployed at B1, B4, and B5. Wave data from B5 were not included in the dataset, as the wave recorder at B5 was damaged during observation, resulting in low data quality. In addition, the buoy at the center of the moored array (B3) was equipped with a visibility meter and Campbell Scientific NR01 four-component net radiation sensor approximately 4 m above the sea surface, with outputs every 1 h, as well as an RBR biochemistry sensor at

https://doi.org/10.5194/essd-2024-224
Preprint. Discussion started: 15 July 2024

the bottom of the buoy (approximately 0 m) with outputs every 12 min. The four-component net radiation sensor recorded shortwave and longwave radiation with upward and downward probes, as well as the wave temperature. The RBR biochemistry sensor recorded the water pressure, turbidity (two probes), chlorophyll, and colored dissolved organic matter. Note that the rope of B3 snapped on September 15, 2014, owing to typhoon Kalmaegi, resulting in the loss of the SBE string at B3, which then became adrift and recovered in October.

A brief demonstration of the observation data at B2, sea surface waves at B1 and B4, and the observations at B3 show that the quality of the data is good and captures several air-sea surface and oceanic processes. Tropical cyclones Rammasun in July, Kalmaegi and Fung-wong in September, and Hagupit in December 2014 traveled over the South China Sea and influenced the time series of the observations. The moored array also experienced a transition from the summer to winter monsoons. In addition, ocean data may have recorded ocean processes, such as near-inertial waves, seasonal variations in temperature, salinity, and currents, as well as background processes, such as mesoscale eddies and local circulations. In summary, this dataset is valuable for further studies to uncover the air-sea interactions and ocean dynamics in the northern South China Sea.

Author Contributions. The dataset is made and the whole manuscript is written by HZ, the whole observation project is designed by DC, the flow of the manuscript is revised by TL and DT, the dataset is optimized by MH, QL and JL.

Competing Interests. The contact author has declared that none of the authors has any competing interests.

Financial support. This work has been supported by the National Key R&D Program of China (2023YFF0805300), the Key R&D Program of Zhejiang Province (2024C03257), the Scientific Research Fund of the Second Institute of Oceanography, MNR (JG2309, QNYC2401), the Project supported by Innovation Group Project of Southern Marine Science and Engineering Guangdong Laboratory (Zhuhai) (316323005), the National Natural Science Foundation of China (42227901, 42176015, 42106008), the National Basic Research Program of China (2013CB430300), the Project supported by Southern Marine Science and Engineering Guangdong Laboratory (Zhuhai) (SML2021SP207, SML2021SP102, SML2022SP401), the MEL Visiting Fellowship (MELRS2303), the Zhejiang Provincial Natural Science Foundation of China (LY24D060003). This research is also supported by the Key Laboratory of Polar Atmosphere-ocean-ice System for Weather and Climate, Ministry of Education, as well as the CMA-FDU Joint Laboratory of Maine Meteorology.

References

Alford, M. H., Peacock, T., MacKinnon, J. A., Nash, J. D., Buijsman, M. C., Centurioni, L. R., Chao, S. Y., Chang, M. H., Farmer, D. M., Fringer, O. B., Fu, K. H., Gallacher, P. C., Graber, H. C., Helfrich, K. R., Jachec, S. M., Jackson, C. R.,

https://doi.org/10.5194/essd-2024-224
Preprint. Discussion started: 15 July 2024

Klymak, J. M., Ko, D. S., Jan, S., Johnston, T. M., Legg, S., Lee, I. H., Lien, R. C., Mercier, M. J., Moum, J. N., Musgrave, R., Park, J. H., Pickering, A. I., Pinkel, R., Rainville, L., Ramp, S. R., Rudnick, D. L., Sarkar, S., Scotti, A., Simmons, H. L., St Laurent, L. C., Venayagamoorthy, S. K., Wang, Y. H., Wang, J., Yang, Y. J., Paluszkiewicz, T., and Tang, T. Y.: The formation and fate of internal waves in the South China Sea, Nature, 521, 65–69, doi:10.1038/nature14399, 2015.

Cai, Z., Gan, J., Liu, Z., Hui, C. R., and Li, J.: Progress on the formation dynamics of the layered circulation in the South China Sea, Prog. Oceanogr, 181, 102246, doi:10.1016/j.pocean.2019.102246, 2020.

Chen, W., Hu, P., and Huangfu, J.: Multi-scale climate variations and mechanisms of the onset and withdrawal of the South China Sea summer monsoon, Sci. China Earth Sci., 65, 1030–1046, doi:10.1007/s11430-021-9902-5, 2022.

Chen, W., Zhang, R., Wu, R., Wen, Z., Zhou, L., Wang, L., Hu, P., Ma, T., Piao, J., Song, L., Wang, Z., Li, J., Gong, H., Huangfu, J., and Liu, Y.: Recent Advances in Understanding Multi-scale Climate Variability of the Asian Monsoon, Adv. Atmos. Sci., 40, 1–28, doi:10.1007/s00376-023-2266-8, 2023.

Guan, S., Jin, F. F., Tian, J., Lin, II, Pun, I. F., Zhao, W., Huthnance, J., Xu, Z., Cai, W., Jing, Z., Zhou, L., Liu, P., Zhang, Y., Zhang, Z., Zhou, C., Yang, Q., Huang, X., Hou, Y., and Song, J.: Ocean internal tides suppress tropical cyclones in the South China Sea, Nat. Commun., 15, 3903, doi:10.1038/s41467-024-48003-y, 2024.

He, Y., Lin, X., Han, G., Liu, Y., and Zhang, H.: The different dynamic influences of Typhoon Kalmaegi on two pre-existing anticyclonic ocean eddies, Ocean Sci., 20, 621–637, doi:10.5194/os-20-621-2024, 2024.

Jilan, S.: Overview of the South China Sea circulation and its influence on the coastal physical oceanography outside the Pearl River Estuary, Cont. Shelf Res., 24, 1745–1760, doi:10.1016/j.csr.2004.06.005, 2004.

Li, J., Zhou, C., Li, M., Zheng, Q., Li, M., and Xie, L.: A case study of continental shelf waves in the northwestern South China Sea induced by winter storms in 2021, Acta Oceanol. Sin., 43, 59–69, doi:10.1007/s13131-023-2150-5, 2024.

Lim Kam Sian, K. T. C., Dong, C., Liu, H., Wu, R., and Zhang, H.: Effects of Model Coupling on Typhoon Kalmaegi (2014) Simulation in the South China Sea, Atmosphere, 11, 432, doi:10.3390/atmos11040432, 2020.

Lin, J., Fang, S., Xu, W., Ni, S., Zhang, H., and Yang, T.: Multi-instrument observations of microseisms generated by typhoon Kalmaegi (2014) over the Northwestern Pacific, Earth Planet. Sci. Lett., 594, 117746, doi:10.1016/j.epsl.2022.117746, 2022.

Liu, Q., Kaneko, A., and Jilan, S.: Recent Progress in Studies of the South China Sea Circulation, J. Oceanogr., 64, 753–762, 2008.

Liu, S.-S., SUN, L., Wu, Q., and Yang, Y.-J.: The responses of cyclonic and anti-cyclonic eddies to typhoon forcing: the vertical temperature-salinity structure changes associated with the horizontal convergence/divergence, J. Geophys. Res. Oceans, 122, 4974–4989, doi:10.1002/2017JC012814, 2017.

Lu, X., Dong, C., Xu, Z., Yang, J., Zhang, H., Wang, D., and Chen, D.: Effects of numerical model's horizontal resolution on the vertical transport of near-inertial energy, Deep-Sea Res. II, 207, 105223, doi:10.1016/j.dsr2.2022.105223, 2023.

Lu, X., Yu, H., Ying, M., Zhao, B., Zhang, S., Lin, L., Bai, L., and Wan, R.: Western North Pacific Tropical Cyclone Database Created by the China Meteorological Administration, Adv. Atmos. Sci., 38, 690–699, doi:10.1007/s00376-020-0211-7, 2021.

Lu, X., Dong, C., Zhang, H., Lim Kam Sian, K. T. C., Yang, J., Xu, Z., Li, G., Wang, Q., Cao, Q., You, Z., and Sommeria, J.: Observational Analysis of Vertical Heat Flux Caused by Typhoon-Induced Near-Inertial Waves Under the Modulation of Mesoscale Eddies, J. Geophys. Res. Oceans, 129, e2024JC021053, doi:10.1029/2024jc021053, 2024.

Ma, Z., Fei, J., Lin, Y., and Huang, X.: Modulation of Clouds and Rainfall by Tropical Cyclone's Cold Wakes, Geophys. Res. Lett., 47, e2020GL088873, doi:10.1029/2020gl088873, 2020.

Nan, F., Xue, H., and Yu, F.: Kuroshio intrusion into the South China Sea: A review, Prog. Oceanogr., 137, 314–333, doi:10.1016/j.pocean.2014.05.012, 2015.

Qi, M., Han, B., Yang, Q., Wu, R., Liu, C., Zhang, G., Zhang, X., Zhou, H., Chen, J., and Chen, D.: Sea Surface Energy Fluxes' Response to the Quasi-Biweekly Oscillation: A Case Study in the South China Sea, Geophys. Res. Lett., 50, doi:10.1029/2023gl104288, 2023.

Quan, Q., Liu, Z., Yang, Y., Cai, Z., Zhang, H., and Liu, X.: Characterization of intraseasonal fluctuations in the abyssal South China Sea: An insight into the energy pathway, Prog. Oceanogr., 206, 102829, doi: 10.1016/j.pocean.2022.102829, 2022.

Shan, K., Chu, P.-S., and Yu, X.: Interdecadal Change of Tropical Cyclone Translation Speed during Peak Season in South China Sea: Observed Evidence, Model Results, and Possible Mechanism, J. Clim., 36, 4531–4541, doi:10.1175/jcli-d-22-0704.1, 2023.

Song, X., Wang, X., Cai, W., and Xie, X.: Observed Air–Sea Turbulent Heat Flux Anomalies during the Onset of the South China Sea Summer Monsoon in 2021, Mon. Weather Rev., 151, 2443–2464, doi:10.1175/mwr-d-22-0314.1, 2023.

Tan, K., Xie, L., Bai, P., Zheng, Q., Li, J., Xu, Y., and Li, M.: Modulation Effects of Mesoscale Eddies on Sea Surface Wave Fields in the South China Sea Derived From a Wave Spectrometer Onboard the China-France Ocean Satellite, J. Geophys. Res. Oceans, 128, doi:10.1029/2021jc018088, 2023.

Wang, Q., Zhang, B., Zeng, L., He, Y., Wu, Z., and Chen, J.: Properties and Drivers of Marine Heat Waves in the Northern South China Sea, J. Phys. Oceanogr., 52, 917–927doi:10.1175/jpo-d-21-0236.1, 2022.

Wang, Q., Zeng, L., Shu, Y., Li, J., Chen, J., He, Y., Yao, J., Wang, D., and Zhou, W.: Energetic Topographic Rossby Waves in the northern South China Sea, J. Phys. Oceanogr., 49, 2697–2714, doi:10.1175/JPO-D-18-0247.1, 2019.

Wu, R., Zhang, H., and Chen, D.: Effect of Typhoon Kalmaegi (2014) on northern South China Sea explored using Muti-platform satellite and buoy observations data, Prog. Oceanogr., 180, 102218, doi:10.1016/j.pocean.2019.102218, 2020.

Xie, X., Liu, Q., Zhao, Z., Shang, X., Cai, S., Wang, D., and Chen, D.: Deep Sea Currents Driven by Breaking Internal Tides on the Continental Slope, Geophys. Res. Lett., 45, 6160–6166, doi:10.1029/2018GL078372, 2018.

Yang, Y., Wang, D., Wang, Q., Zeng, L., Xing, T., He, Y., Shu, Y., Chen, J., and Wang, Y.: Eddy-Induced Transport of Saline Kuroshio Water Into the Northern South China Sea, J. Geophys. Res. Oceans, 124, 6673–6687, doi:10.1029/2018jc014847, 2019.

Ying, M., Zhang, W., Yu, H., Lu, X., Feng, J., Fan, Y., Zhu, Y., and Chen, D.: An Overview of the China Meteorological Administration Tropical Cyclone Database, J. Atmos. Oceanic Tech., 31, 287–301, doi:10.1175/jtech-d-12-00119.1, 2014.

Zhang, H.: Modulation of Upper Ocean Vertical Temperature Structure and Heat Content by a Fast-Moving Tropical Cyclone, J. Phys. Oceanogr., 53, 493–508, doi:10.1175/JPO-D-22-0132.1, 2023.

Zhang, H., Chen, D., Tongya, L., Tian, D., He, M., Li, Q., and Liu, J.: A Moored Array Observation Dataset for Air-Sea·Surface, Upper and Bottom Ocean in the Northern South China Sea during 2014-2015 (MASCS 1.0) [Data set]. Zenodo. doi: 10.5281/zenodo.12635331, 2024.

Zhang, H., Chen, D., Zhou, L., Liu, X., Ding, T., and Zhou, B.: Upper ocean response to typhoon Kalmaegi (2014), J. Geophys. Res. Oceans, 121, 6520–6535, doi:10.1002/2016jc012064, 2016.

Zhang, H., Wu, R., Chen, D., Liu, X., He, H., Tang, Y., Ke, D., Shen, Z., Li, J., Xie, J., Tian, D., Ming, J., Liu, F., Zhang, D., and Zhang, W.: Net Modulation of Upper Ocean Thermal Structure by Typhoon Kalmaegi (2014), J. Geophys. Res. Oceans, 123, 7154–7171, doi:10.1029/2018JC014119, 2018.